

---

This item was submitted to [Loughborough's Research Repository](#) by the author.  
Items in Figshare are protected by copyright, with all rights reserved, unless otherwise indicated.

## Asperity level tribological investigation of automotive bore material and coatings

PLEASE CITE THE PUBLISHED VERSION

<https://doi.org/10.1016/j.triboint.2017.08.023>

PUBLISHER

© The Authors. Published by Elsevier Ltd.

VERSION

VoR (Version of Record)

PUBLISHER STATEMENT

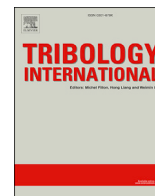
This work is made available according to the conditions of the Creative Commons Attribution 4.0 International (CC BY 4.0) licence. Full details of this licence are available at: <http://creativecommons.org/licenses/by/4.0/>

LICENCE

CC BY 4.0

REPOSITORY RECORD

Umer, Jamal, Nick Morris, Michael Leighton, Ramin Rahmani, S.J. Howell-Smith, R. Wild, and Homer Rahnejat. 2019. "Asperity Level Tribological Investigation of Automotive Bore Material and Coatings". figshare. <https://hdl.handle.net/2134/26346>.



## Asperity level tribological investigation of automotive bore material and coatings



J. Umer<sup>a</sup>, N. Morris<sup>a</sup>, M. Leighton<sup>a</sup>, R. Rahmani<sup>a,\*</sup>, S. Howell-Smith<sup>b</sup>, R. Wild<sup>b</sup>, H. Rahnejat<sup>a</sup>

<sup>a</sup> Wolfson School of Mechanical, Electrical and Manufacturing Engineering, Loughborough University, Loughborough, UK

<sup>b</sup> Capricorn Automotive Ltd, Basingstoke, UK

### ARTICLE INFO

#### Keywords:

Cylinder bore material  
Nano-scale friction  
Atomic force microscope  
Lateral force mode

### ABSTRACT

Choosing in-cylinder surfaces is complex. A well-chosen surface has low friction and wear. Conversely, poor oversight often leads to premature failure through wear and scuffing. Typically cylinder bore surfaces are selected experientially. This paper demonstrates the use of Atomic Force Microscopy in LFM mode, characterising typical cylinder bore materials and coatings. The approach uses integrated LFM with continuum contact mechanics. It evaluates the real contact area and effective elastic modulus of the surface, including the effect of any reactive surface film. Surface energy and shear strength, as well as the coefficient of friction in nanoscale interactions are also determined. These properties are measured for 6 cylinder bore materials, including for composite Nickel-Silicon Carbide and DLC, used for high performance engines.

### 1. Introduction

Environmental pollution is a growing global concern. The road transport sector is a major contributor to this problem. Therefore, improving the efficiency of automotive powertrain systems is viewed as a pertinent palliative measure, which is subject of a growing list of legislation and directives [1]. The harmful emissions are partly as a result of internal combustion engine frictional losses. These have been shown to account for 15–20% of the fuel consumed in internal combustion powered road vehicles [2]. Under challenging inner city or urban drive cycles these losses can rise to as much as 20–30% of all the expended fuel energy [3]. A significant part of engine frictional losses (40–50%) is due to piston-cylinder system [4,5]. As a result, significant changes are made in engine design at a system level. These include new technologies such as Cylinder De-Activation (CDA) in a drive to improve fuel efficiency [6], leading to reduced levels of harmful emissions, particularly in urban driving conditions. However, the increasingly harsh operating conditions in modern engines exacerbate frictional power losses irrespective of the introduced new technologies such as CDA. The expected optimal outcomes are not realised as shown by Bewsher et al. [7] for the effect of CDA on piston compression ring-cylinder liner contact and by Mohammadpour et al. [8] for the case of connecting rod bearings. Therefore, another trend is to improve cylinder bore and piston and rings' surfaces in

terms of topography [9–11], coatings [12–14] and other surface treatments such as surface texturing [15–17] for enhanced frictional performance, as well as for wear resistance. All of these are intended outcomes against the prevailing trend in light-weight and durable powertrain technologies. An example of this has been the move away from tribologically advantageous Cast Iron (CI) engine blocks towards low weight aluminium alloys, necessitating the development of cylinder liner inserts or application of direct coatings.

Selecting running surfaces is a significant challenge for engine specialists, tribologists and material scientists alike. Identification of appropriate surfaces is typically conducted in an empirical manner or through mimicry of tried and tested exemplars found in current engineering practice [18]. The difficulty of surface selection is two-fold. Firstly, friction and wear are inherent system attributes. Secondly, coatings or substrate materials are required to achieve a complex and often contradictory set of design objectives. Therefore, it is pertinent at this point to specify the conjunctive configuration and contact conditions which the intended work aims to focus upon in order for functional requirements of the surfaces/coatings to be ascertained.

The piston, ring and cylinder sub-system is a reciprocating, partially conforming contact subject to varying transient kinematics and loading. Boundary friction has been shown to dominate at piston reversals due to the momentary cessation of lubricant entrainment [11,19–22].

\* Corresponding author.

E-mail address: [R.Rahmani@lboro.ac.uk](mailto:R.Rahmani@lboro.ac.uk) (R. Rahmani).

<http://dx.doi.org/10.1016/j.triboint.2017.08.023>

Received 29 June 2017; Received in revised form 17 August 2017; Accepted 24 August 2017

Available online 4 September 2017

0301-679X/© 2017 The Authors. Published by Elsevier Ltd. This is an open access article under the CC BY license (<http://creativecommons.org/licenses/by/4.0/>).

Nomenclature			
$a$	Contact radius [m]	$\delta$	Elastic compression of contacting pair [m]
$A$	Contact area [m <sup>2</sup> ]	$\delta_C$	Cantilever deflection [m]
$C$	Calibration factor [–]	$\epsilon$	Adhesion hysteresis (fraction) [–]
$E$	Elastic modulus [Pa]	$\theta$	Contact angle [°]
$F_{ad}$	Surface adhesion [N]	$\tau$	Interfacial shear strength [Pa]
$F_f$	Friction [N]	$\gamma$	Surface energy [J/m <sup>2</sup> ]
$F_m$	Meniscus force [N]	$\nu$	Poisson's ratio [–]
$F_N$	Normal contact force [N]	<b>Abbreviations</b>	
$k_C$	Cantilever stiffness [N]	AFM	Atomic Force Microscope
$E^*$	Reduced modulus of elasticity [Pa]	CDA	Cylinder De-Activation
$L$	Measured contact Load [N]	CI	Cast Iron
$L_p$	Measured pull-off force [N]	DLC	Diamond Like Carbon
$\bar{P}$	Dimensionless Load Parameter [–]	DMT	Derjaguin-Muller-Toporov
$R$	AFM tip radius [m]	FeMo	Iron Molybdenum
$R_{pk}$	Reduced peak height [m]	FE-SEM	Field Emission Scanning Electron Microscope
$w$	Work of adhesion	LFM	Lateral Force Mode
$z_0$	Atomic equilibrium separation [m]	Ni-SiC	Nickel-Silicon Carbide; PEO Plasma Electrolytic Oxide
<b>Greek Letters</b>		RMS	Root Mean Square
$\alpha$	AFM cantilever holder angle [°]	$R_{pk}$	Peak height roughness
		TiO <sub>2</sub>	Titanium Dioxide

Therefore, some direct contact of bounding contacting solids would occur, where the generated friction is directly affected by surface material and topography. This is particularly the case at the top dead centre reversal as high cylinder liner temperatures reduce the lubricant's load carrying capacity [23] and during the power stroke when in-cylinder pressure increases the radial load against the cylinder bore. Reducing the generated boundary friction, created by interacting asperity pairs on the counter face surfaces and any intermediary adsorbed layer, is the key to improving engine efficiency. One method of achieving this is through use of suitable coating on the contacting surfaces to guard against wear, whilst reducing boundary friction [13,14,18,24].

The use of bench top tribometers has been shown as an effective method to compare coating performance. A comparison of reciprocating sliding tribometer performance and engine fuel economy for various lubricant-surface combinations has shown a strong correlation [25,26]. Gore et al. [26] compared two running surfaces using a bench-top tribometer and an analytical model. Measured data from Atomic Force Microscopy (AFM) was used in the analytical model to characterise the materials' boundary shear strength. The model was shown to accurately benchmark the performance of various surface materials.

Lateral Force Mode (LFM) with AFM has enabled measurement of friction at the asperity level for dry and lubricated surfaces [27–29]. AFM has also been frequently used to investigate the nano-mechanical and nano-tribological properties of coatings [24,29–32]. AFM has been shown to provide an insight into the failure mechanism of thin coatings [33]. Carpick et al. [34] have shown that nano-scale frictional properties are functions of AFM tip radius, reduced elastic modulus, adhesion and interfacial shear strength.

For automotive coatings, characterisation and measurement by means of scratching (wear), indentation (hardness) and mechanical (elastic modulus) are quite commonplace. Direct comparison by means of LFM for various materials is less common. This paper documents the use of LFM for nano-scale elastic modulus measurement as well as contact mechanics analysis as part of a selection procedure for cylinder liner surface material. The procedure benchmarks surface coatings in relation to frictional properties at asperity interaction level. The results provide useful information for mechanical characterisation of the running contacting surfaces, specific to automotive piston-cylinder application. Such an approach has not hitherto been reported in literature.

## 2. Mechanics of contact

At the interface of the AFM tip-to-a sample surface conjunction, there exists a combination of active kinetics, such as meniscus and adhesive forces. Thus, the mechanics of the contact deviates from the classical Hertzian theory. The adhesive forces are promoted by the short range surface forces of the materials, for which the continuum models proposed by Bradley [35], Johnson et al. [36], Derjaguin et al. [37] and the broader Maugis model [38] may be employed. To determine the applicability of these models two non-dimensional parameters are used [39]. Firstly, an elasticity parameter  $\mu$  is used, which represents the ratio of elastic deformation resulting from adhesive disengagement from a surface to a range of surface forces [40]:

$$\mu = \left( \frac{Rw^2}{E^*z_0^2} \right)^{1/3} \quad (1)$$

where,  $R$  is the reduced radius of contacting bodies (in this case the tip radius of the AFM probe against a flat specimen surface),  $w$  is the work of adhesion,  $z_0$  is the atomic equilibrium separation and  $E^*$  is the reduced (equivalent) modulus of elasticity of the contacting pair:

$$E^* = \left( \frac{1 - \nu_1^2}{E_1} + \frac{1 - \nu_2^2}{E_2} \right)^{-1} \quad (2)$$

where,  $\nu$  and  $E$  are the poisson's ratio and Young's modulus of elasticity of the contacting surface respectively. The second parameter is to determine the most appropriate adhesion model. This is the dimensionless load parameter  $\bar{P}$ , which is the ratio of the applied normal force,  $F_N$ , to the adhesive force:

$$\bar{P} = \frac{F_N}{\pi w R} \quad (3)$$

where,  $w$  is the work of adhesion.

Preliminary investigation of a candidate surfaces, subject of this investigation yielded load parameters in the range 10–100 and the dimensionless elasticity parameter in the range 0.005–0.05. Using The Adhesion Map in Ref. [39], it can be shown that the most appropriate contact mechanics theory for the contact of the silicon nitride AFM tip to

the samples used in this investigation is that due to Derjaguin et al. [37], known as the DMT model. This is an expected outcome due to the small tip radius and relatively hard surfaces with low adhesive forces, an outcome which is consistent with the findings of Enachescu et al. [41] for similar materials.

A brief description of the DMT theory [37] and its link to the interfacial friction is provided here.

The DMT theory follows the classical Hertzian theory to determine the localised elastic deformation of the contacting surfaces in addition to the inclusion of adhesive surface force, thus:

$$F_N = -F_{ad} + \frac{4}{3}E^* \sqrt{R} \delta^{3/2} \quad (4)$$

where  $F_{ad}$  is the adhesive force and  $\delta$  is the contact deflection of the surfaces. Friction has been shown to be related to the contact area and the interfacial shear strength of the contacting surfaces, thus the contact half width,  $a$ , can be written as:

$$a = \sqrt[3]{\frac{3R(F_N - F_{ad})}{4E^*}} \quad (5)$$

Bowden and Tabor [42] presented their plastic junction theory of friction when ploughing of asperities occurs, proportionally to the real contact area. This has been shown to be the case for contact half-widths as diminutive as 2 nm by Lantz et al. [43]. This can be written in terms of contact area,  $A$ , and the boundary shear strength of the surface,  $\tau$  as:

$$F_f = \tau A = \tau \pi a^2 \quad (6)$$

$$F_f = \tau A = \tau \pi \left[ \frac{3R(F_N - F_{ad})}{4E^*} \right]^{2/3} \quad (7)$$

When using an AFM in a normal humid atmosphere the contribution of meniscus force due to condensation on the surface of specimen should not be discounted. A mono-layer of water molecules forms on any surface within 25  $\mu$ s and grows exponentially thereafter [44,45]. In the current study the relative humidity in the measurement chamber was 50 $\pm$ 5% RH. At this level of relative humidity, it has been shown that for non-polar condensed film, such cyclohexane, the bulk parameters can be used to describe the capillary action [46]. However, hydrogen bonds present in condensed aqueous films require a meniscus radius greater than 1.5 nm for liquid phase bulk parameters to be applicable [47]. While the direct measurement of condensed film thickness and meniscus radii is outside the scope of the present work; similar models have been employed to effectively explain experimental results for very similar environments and contact conditions [48,49]. Therefore, for the conditions in the current study it is deemed reasonable to employ bulk parameter models, inter alia, surface tension observable at microscopic level in order to model capillary forces at the scale of the AFM tip.

The contact angle of a water droplet on all specimen surfaces is measured through goniometry. The meniscus force,  $F_m$ , can then be determined through thermodynamic equilibrium on assumed smooth surfaces [50] as:

$$F_m = -2\pi R \gamma_{lv} (\cos \theta_1 + \cos \theta_2) \quad (8)$$

where,  $\theta_1$  is the contact angle of water with the silicon nitride AFM tip and  $\theta_2$  is that of water with each specimen used in the study, while  $\gamma_{lv}$  is the liquid-vapour surface energy. The measured values are listed in Table 2. The meniscus force is used to find the normal applied contact load,  $F_N$  from the measured force,  $L$  as:

$$F_N = L - F_m \quad (9)$$

The experimentally determined pull-off or detachment force,  $L_p$  comprises the meniscus force,  $F_m$  and the surface (adhesive) force,  $F_{ad}$ . Assuming two rigid surfaces, their relationship can be expressed as:

$$F_{ad} = L_p - F_m \quad (10)$$

The surface energy,  $\gamma$ , can be determined from the adhesive component of the pull-off force as:

$$\gamma = -\frac{4\pi R}{F_{ad}} \quad (11)$$

### 3. Experimental measurements

LFM is used to measure and benchmark the frictional performance of six specimen materials, which are most commonly used as the primary working cylinder bore/liner surfaces for a wide range of internal combustion engines. The chosen materials/coatings have a range of surface hardness with various levels of densification (i.e. certain bore surface materials contain porosity such as cast iron and FeMo). Surface images for the prepared samples are provided in Fig. 1, using a LEO 1530-VP high resolution Field Emission Scanning Electron Microscope (FE-SEM). The image area considered was 55  $\times$  30  $\mu$ m<sup>2</sup>. These provide a qualitative analysis of the material/coating thickness with surface features in the sub-micrometre scale. Typical regional topography measurements are also provided using AFM over a 1  $\times$  1  $\mu$ m<sup>2</sup> area.

All 6 specimens are prepared as flat samples, with dimensions: 100  $\times$  50  $\times$  8 mm, and with ground working surfaces, followed by flat lapping to an overall flatness tolerance of 10  $\mu$ m. The topography is subjected to further finishing process described below. Commonly engine bore surfaces are plateau honed to improve tribological performance. The focus of the current study is on the surface material performance rather than its surface finish. For this reason a much smoother isotropic surface has been generated, which is particularly suitable for measurements with AFM.

In preparation of all sample materials, care is taken to achieve similar asperity morphology in order to minimise the differences in their frictional performance which may be attributed to boundary friction contribution through asperity ploughing. This action confines, as far as possible, the mechanism of generated friction to adhesion, thus becomes a representative benchmarking method for specimen surface materials in contact with the same counter face surface (in this case the silicon nitride tip of the AFM probe). Other investigations using different specimens have shown that the effect of ploughing friction as the result of their widely varying surface topographies prohibits direct comparison of counter face surface material combinations [51]. The minimisation of the effect of different asperity ploughing levels also improves the validity of the highlighted analytical method described in section 2. Therefore, diamond paste polishing is used at the surface finishing stage. The DLC coated sample presents a particular challenge in this regard as there is a limit to the substrate surface roughness prior to coating in order to minimise spalling due to internal stresses set up by coating conformity to rough surface topographies.

In addition, DLC produces surfaces of increased roughness post coating. The substrate material for the DLC coating was lapped using Kemet 6  $\mu$ m polycrystalline diamond which satisfies the roughness limitations for coating adhesion. Post coating, the surface roughness was measured and a 30% increase in  $R_{pk}$  was encountered. Each sample was measured 6 times, with an evaluation length of 1.775 mm and a length cut-off length of 0.225 mm. Kemet 9  $\mu$ m polycrystalline diamond polishing compound was found to provide near equivalent roughness to the post coated DLC specimen, when applied to the electroplated nickel-silicon carbide (Ni-SiC2) specimen. All the surfaces presented in Table 1, with the exception of DLC, were therefore finally lapped using a 9  $\mu$ m polycrystalline diamond polishing compound.

Due to the differing nature of the prepared surfaces (differential porosity), significant variation is noted and indeed expected for surface roughness due to the inherent contribution of roughness valleys. The use of same grade abrasive is justified on the basis of similar asperity

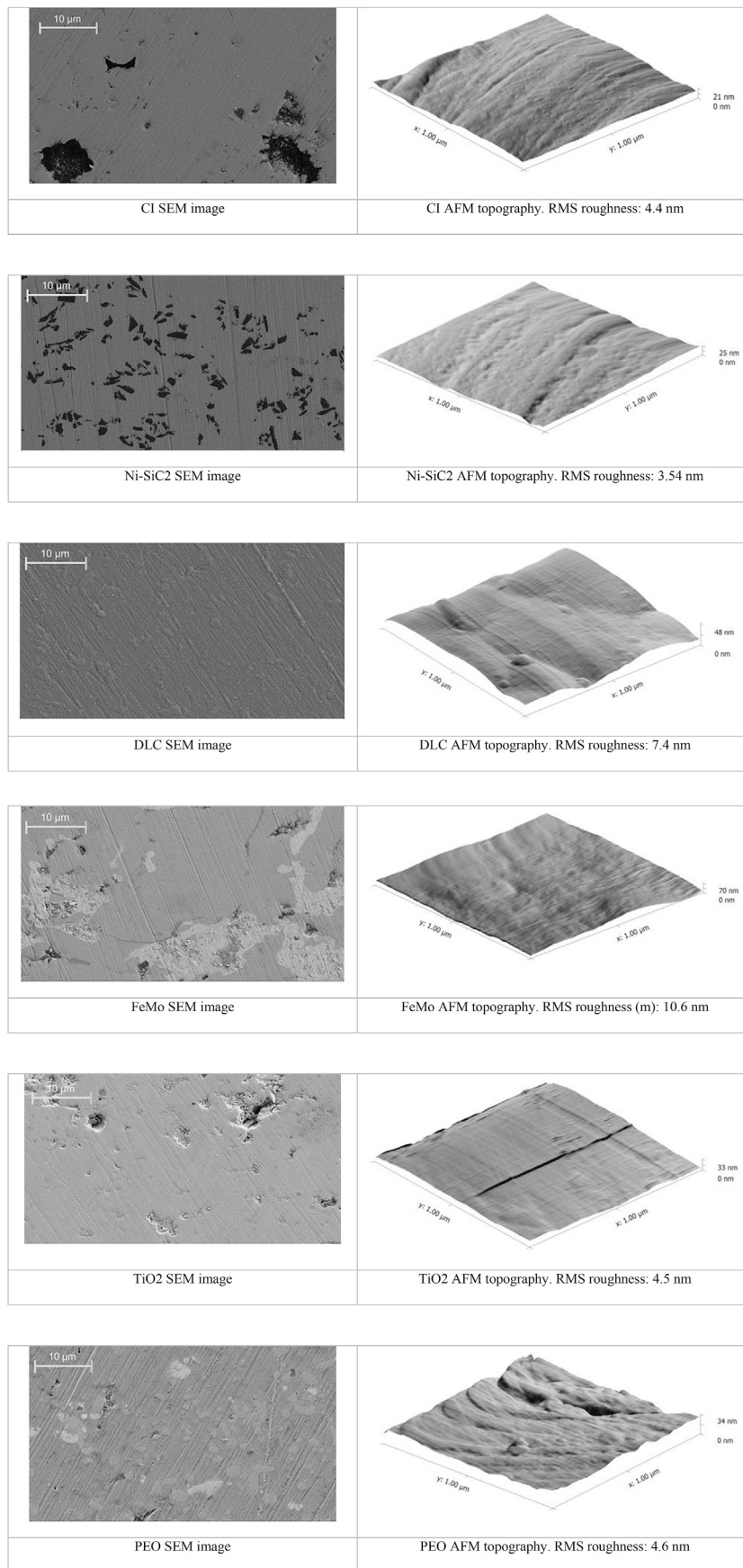


Fig. 1. SEM images of prepared sample surfaces with AFM topographical images and measurements.

Table 1  
Sample data.

Sample	CI	Ni-SiC2	DLC	FeMo	TiO2	PEO
Base material	ASTM-A48, Class 30 Centrifugally cast grey iron	BS970: 1991 817M40T Alloy steel quenched and tempered	BS970: 1991 817M40T Alloy steel quenched and tempered	BS970: 1991 817M40T Alloy steel quenched and tempered	BS970: 1991 817M40T Alloy steel quenched and tempered	AA 4032 T6 Aluminium alloy solution treated and artificially aged
Surface Coating	Surface finish as lapped R <sub>pk</sub> (RMS) [nm]: Coating:	N/A	N/A	N/A	N/A	N/A
	Surface finish as deposited R <sub>pk</sub> (RMS) [nm]: Surface finish as lapped R <sub>pk</sub> (RMS) [nm]: Thickness as finished [μm]	Electroplated nickel with co-deposited silicone particulate N/A	Thin film vacuum deposited diamond like carbon 22 - 42 (7.4)	High energy thermally sprayed iron and molybdenum N/A	High energy thermally sprayed titanium dioxide N/A	High energy 'plasma' anodised N/A
	N/A	15 - 20 (3.5)	N/A	63 - 277 (10.6)	31 - 148 (4.5)	56 - 75 (4.6)
	N/A	70	2	400	400	10

Table 2

Measured elastic moduli and water contact angles for all sample materials.

Material Description	Elastic Modulus (GPa)	Contact angle (°)
CI	99 ± 6	78 ± 1.2
Ni-SiC2	109 ± 4	94 ± 0.3
DLC	180 ± 3	68 ± 1.8
FeMo	149 ± 2	84 ± 2.3
TiO2	165 ± 3	73 ± 0.8
PEO	92 ± 5	84 ± 0.6
(AFM Tip material) silicon nitride	310 <sup>a</sup>	47 <sup>b</sup>

<sup>a</sup> Reported by the manufacturer.

<sup>b</sup> Reported by Agarwal et al. [55].

generation for the prepared surfaces.

### 3.1. Lateral force microscopy

The surface topography and frictional characteristics of various surfaces and coatings are investigated using a Veeco Dimensions-3100 Atomic Force Microscope. The samples are subjected to LFM by a Bruker DNP-10 non-conductive silicon nitride tip, held on a silicon nitride cantilever. The tip has a nominal radius of 20 nm. The cantilever stiffness is 0.06 N/m. The low stiffness is used to avoid plastic deformation of scanned surfaces, which would occur with excessive contact pressures. To guard against this outcome, the normal applied loads are limited to 50 nm. Further verification with regard to the prevailing elastic nature of the contact is provided later in section 3.2.

The cantilever and tip are calibrated before each measurement in order to ensure a high level of measurement repeatability. The accuracy of the results is strongly dependent on this process [48]. A silicon nitride sample with known frictional properties is used for the calibration process, using the blind calibration method [24,51–53]. The coefficient of friction of the standard silicon nitride sample is 0.19 [51].

The normal measured applied load *L* is determined by multiplying the applied load in Volts by the slope of the force-distance curve for a known cantilever spring constant. A 1 × 1 μm area of the calibration sample is scanned with a frequency of 2 Hz with a sample array of 256 × 256 points. Average friction *F<sub>f</sub>* is recorded in Volts using the trace-minus-retrace method. All experiments are carried out in a controlled ambient condition (20 ± 2 °C, and 50 ± 5% RH).

The calibration factor *C<sub>F</sub>* for the tip used is calculated as [52].

$$C_F = \frac{F_f[V]}{L[nN]} \times 0.19 \quad (12)$$

The calibration factor is determined through curve fitting for a range of measured normal applied loads and curve fitted (an example is shown in Fig. 2). The resulting equation predicts the response of the AFM tip assembly over the range of test loads. The error bars represent the standard deviation of the measurement used for the calibration procedure which is repeated for each tip used.

Friction for the samples is calculated as:

$$F_f[nN] = F_f[V]/C_F \quad (13)$$

For each sample and at any applied load 4 measurements are carried out. The error bars in Fig. 3 show the degree of scatter in the measurements.

### 3.2. Measurement of modulus of elasticity

LFM testing of samples is carried out with the AFM in the above stated controlled ambient conditions. With a layer of moisture assumed to be present on the surface of samples, combined with applied pressure and shear, as well as generated contact heat a reactive thin layer including various material oxides would be formed on the specimen surfaces. This affects the contact surface elastic modulus, which is required for the

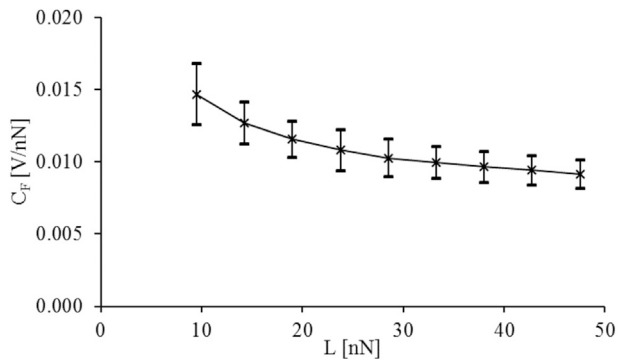


Fig. 2. Example calibration of Bruker DNP-10 tip with a standard AFM silicon nitride calibration sample.

analysis of measurements highlighted in the aforementioned analytical method (section 2). Therefore, measurement of Young's modulus of elasticity of the specimen surface is essential, as well as the real area of contact and its shear strength. Carpick et al. [54] state that the determination of the real area of contact is the key parameter in determining the frictional behaviour at the nano-scale. The elastic modulus is linked to the material's constitutive relations and is a necessary parameter for determining contact deflection and the real contact area. It has been shown that the contacting surfaces evolve into a complex graded structure of both counter face materials' composition and mechanical properties [55]. As a result surface deflections similar to those encountered in LFM are necessary to obtain representative results, which are in nano-scale as opposed to deflections of a few micrometres commonly used with indentation techniques [56]. Consequently, low normal applied loads should be used to maintain the contact behaviour true to the underlying assumptions of the DMT theory.

In the current study, a Bruker RTE5P-525 rectangular cantilever with a stiffness of 200 N/m and a nominal tip radius of 8 nm is employed to obtain the elastic modulus of the specimen surfaces. The tip radius is measured using a calibrated artefact of known geometry and a deconvolution procedure. Using a cantilever with comparable stiffness to that of the surface facilitates a discernible magnitude of cantilever deflection. The extent of cantilever deflection relative to the measurement system is of importance with regard to the accuracy of the measurements. The deflection of the surface can be determined from the difference between the cantilever height and its deflection. The stiffness of the cantilever and its deflection allow for the true applied normal load to be determined as:

$$L = \frac{k_C \delta_C}{\cos^2(\alpha)} \quad (14)$$

where,  $\alpha$  is the inclination angle of the cantilever, which for the current study is  $10^\circ$  [57].

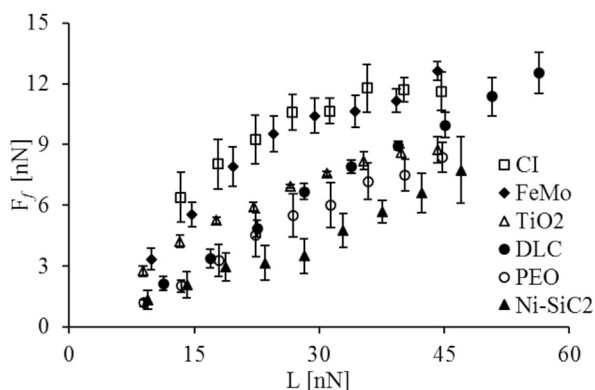


Fig. 3. Friction at various normal applied loads for all samples.

As the normal force and deflection of the surface are both known, the elastic modulus of the surface can be determined through use of the DMT theory. The normal contact load  $F_N$  can be determined from the measured contact load  $L$ , using equation (9). By rearranging equation (4) the reduced elastic modulus is then determined from the surface deflection and the normal contact force as:

$$E^* = \frac{3}{4} \frac{(F_N - F_{adh})}{\sqrt{R\delta^3}} \quad (15)$$

As this process is quite sensitive to surface material inhomogeneity, the measurement process is repeated 4 times for each sample at different locations. The measured reduced elastic moduli for all samples are listed in Table 2. An example result for the CI sample is shown in Fig. 4.

The average reduced elastic modulus for the CI sample across all the measurements taken is 99 GPa. Higher than average values are observed at the very top region of the surface (0–0.5 nm) which is likely to be due to the formation of an oxide layer [55]. The average elastic modulus across this region is then put back into the DMT model to provide a visual demonstration of the goodness of fit of the theory to the measured data (Fig. 5).

#### 4. Results and discussion

Table 2 lists the measured moduli of elasticity of all specimen materials. As already noted, measurements are carried out at 4 locations for each specimen. The average value for each surface material type is provided in the table with standard deviations of the measurement from the average value. The table also includes the average measured contact angle of water with each surface material/coating (obtained through goniometry in normal atmosphere) with the corresponding measurement deviations. The data for the silicon nitride tip are obtained from elsewhere [58].

The relationship between friction and contact area for all the tested specimen surfaces is shown in Fig. 6. The contact area is calculated using equations (5) and (8–10). The graphs show near linear relationship between the measured friction and the predicted contact area, using the DMT theory. The gradient of a line with a zero intercept provides the interfacial shear strength of the contacting pairs. Whilst most of the linearly-fitted data appear to reside on lines with a zero intercept, there are implied deviations from this trend for some of the results. The continuum mechanics theory followed here requires that the intercept of the graphs should be zero. This means that without a contact, there should be no generated friction. For this reason a fixed intercept of zero is chosen for the graphs in Fig. 6. Disagreement with this at the lower contact areas is assumed to be due to a breakdown of the continuum mechanics theory reported for other researchers as well, such as by Lantz et al. [43]. A  $4 \text{ nm}^2$  contact area is equivalent to a 1 nm contact footprint radius, where

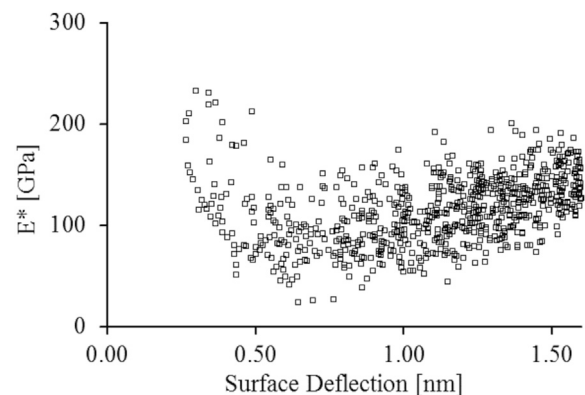


Fig. 4. Determining the reduced Elastic modulus of CI sample at varying surface compliance.

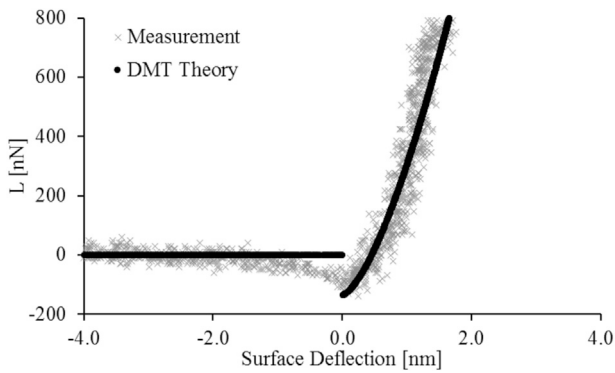


Fig. 5. Comparison of DMT theory with the measured using the reduced elastic modulus value predicted in the previous step.

only a few atoms would reside.

A comparison of the best fit lines (Fig. 6a–f) is shown in Fig. 7. The surfaces with the highest interfacial shear strength are those with the

steepest gradient. It can be observed that Ni-SiC2 surface has the lowest interfacial shear strength, whilst the FeMo and DLC have the highest. The interfacial shear strength of the surface pairs range from 0.51 to 1.4 GPa, which is high compared with typical bulk shear stress parameters of similar materials. This can account for the strong nature of the surface oxide bonds formed on the specimen surfaces [54]. Those with the highest shear strength would have superior wear resistance, but poorer frictional performance. This is an important finding, indicating that wear and friction performance of surface material do not always coincide as is traditionally suggested. With the usual micro-scale topography of in-cylinder surfaces any increased surface shear strength would promote increased boundary friction due to asperity ploughing. This is confirmed through benchmark engine testing of cylinder liner surfaces made of DLC and Ni-SiC2 by Howell-Smith et al. [14], where poorer frictional performance was noted for the DLC coated advanced cylinder liners. Similar findings have also been reported by Demas et al. [59].

Referring to equation (7) it can be seen that there are three key material parameters influencing the nanoscale friction. These are the elastic modulus, interfacial shear strength and adhesion. Fig. 8 shows the variation of mean coefficient of friction with these governing material

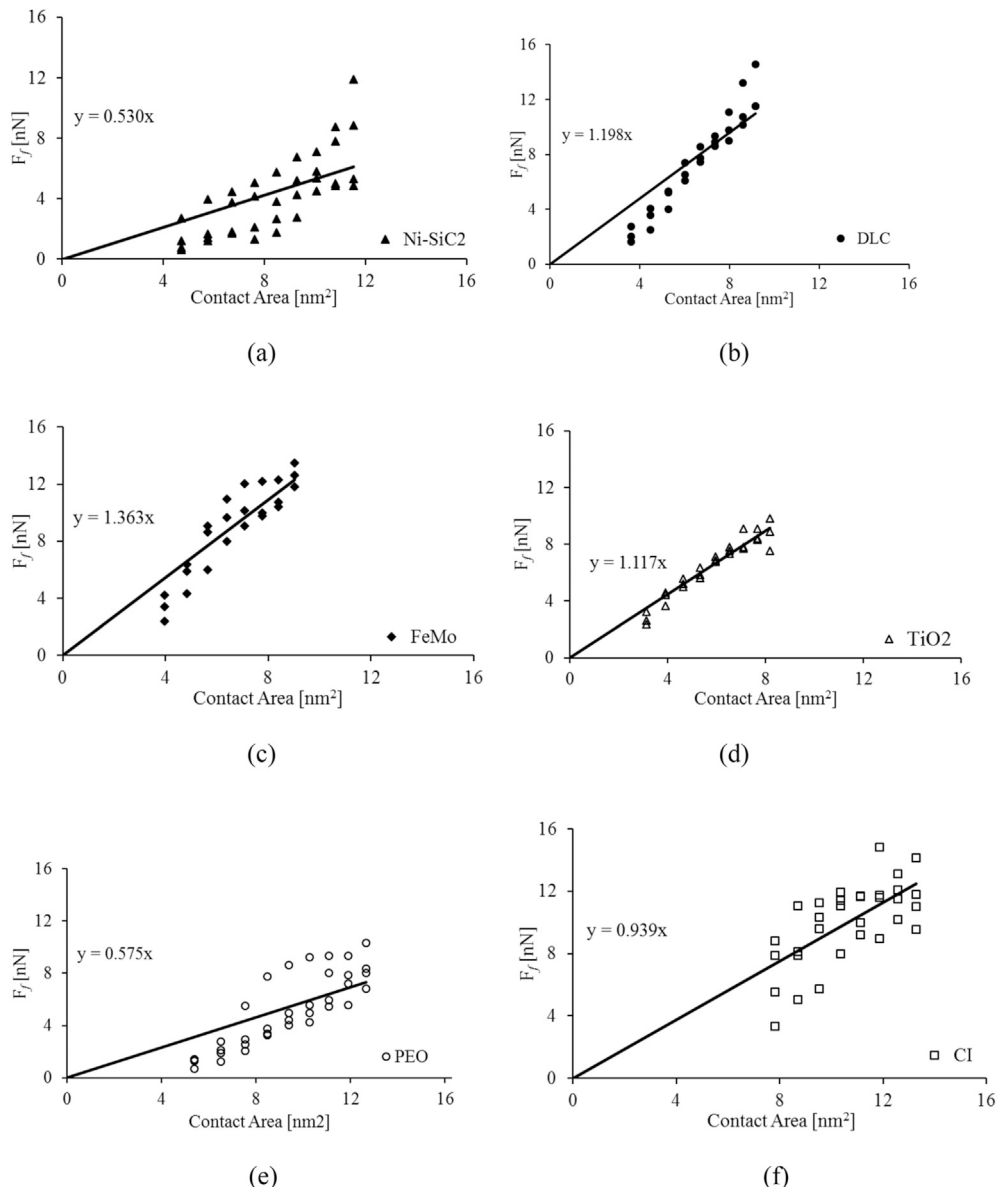


Fig. 6. Friction-real contact area relationship for different surface materials.

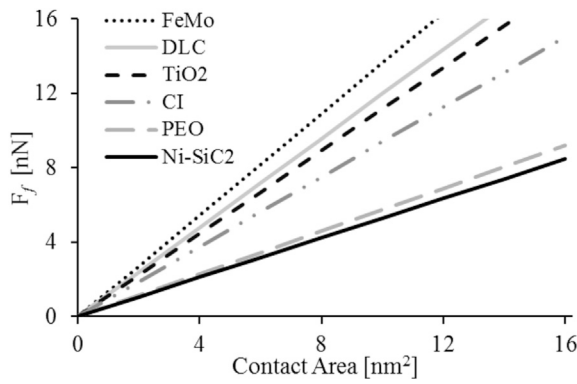


Fig. 7. Comparison of friction variation with real contact area for different sample surfaces.

parameters in equation (7). A clear trend can be observed for all test surface materials. It can be seen that friction is inversely proportional to surface elastic modulus, as the result of the dependence of friction on the real area of contact, as also shown by Carpick et al. [54].

The approximate interfacial shear strength of the contact can be determined using the cobblestone model proposed by Tabor [60] and developed by Sutcliffe et al. [61]. Assuming that some fraction,  $\epsilon$  of the total adhesion energy is dissipated as heat during sliding (i.e. adhesion hysteresis), Homola et al. [62] have shown that the interfacial shear strength of the contact can be approximated by:

$$\tau = \frac{F_f}{A} = \epsilon \left( \frac{2\gamma}{Z_0} \right) \quad (16)$$

where  $Z_0$  is the equilibrium atomic spacing, indicating the lateral distance moved (dislocation) to initiate sliding motion. Using an approximate value of  $Z_0 = 0.1$  nm, a typical surface energy of  $\gamma = 0.03$  N/m and  $\epsilon = 0.5$  (a value which can vary between 0 and 1), it can be seen that:  $\tau \approx 0.3$  GPa. This provides a useful order of magnitude check for the contact shear strength found through LFM and the contact mechanics theory used here. The result in Fig. 8 supports the hypothesis of linearly varying surface energy and shear stress. The surface energy is determined through application of equations (8), (10) and (11).

The results shown in the figure corresponds to the relationship for calculated surface energy (using the measured pull-off force) with the interfacial shear strength of the surfaces. The near linear relationship of the two parameters indicates that the theory embodied in equation (16) provides a reasonable explanation of the results presented. Variations of the interfacial shear strength of the surfaces at similar values of surface energies can be explained through the differences in the adhesion hysteresis parameter ( $\epsilon$ ).

Fig. 9 shows that the Ni-SiC2 surface has the lowest coefficient of friction of all sample surfaces due its low shear strength. With coated

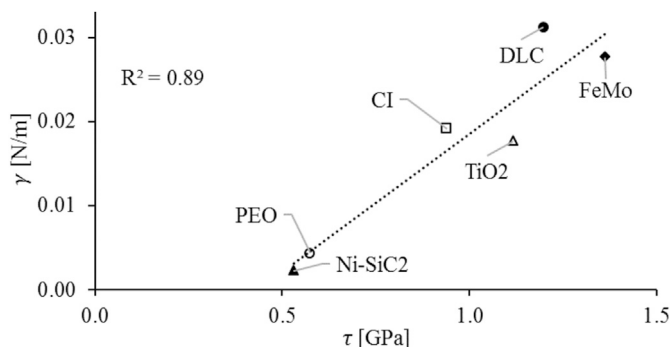


Fig. 8. Surface energy and interfacial shear strength for all samples.

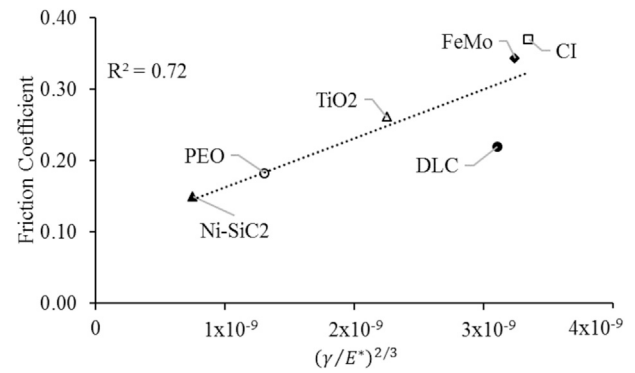


Fig. 9. Friction coefficient of all samples with controlling material parameters.

surfaces care must be taken that a high tensile/alternating stress field does not occur at substrate-coating interface as this can lead to exfoliation of the coating. Light applied loads in the current study guards against this potential surface failure. However, it would be prudent to couple the current approach with appropriate wear and fatigue tests for a complete understanding of surface performance.

The DLC coating attains a middle rank position within this analysis. However, DLC seems to reside outside the linear relationship shown in Fig. 9. The use of  $(\gamma/E^*)^{2/3}$  parameter on the abscissa presumes that surface energy is material-specific, thus affecting the magnitude of interfacial shear strength of the surfaces. This assumption is shown to be reasonable in Fig. 8 for most of the tested material surfaces. Equation (16) shows that the interfacial shear strength is also dependent on the equilibrium atomic spacing and the adhesion hysteresis parameter. From literature it can be seen that the equilibrium spacing of carbon is approximately 40pm in graphite [64], whilst for other surfaces such as TiO2 and Fe crystals, this is 10 – 20 pm and 23 p.m. respectively [65, 66]. It is suggested that whilst the ratio  $\epsilon/Z_0$  may be reasonably constant for most surfaces leaving the surface energy as the material dependent parameter, the same cannot be assumed for the case of DLC. Evidentially further investigation of the dissipative processes involved would still be required.

It is important to note its significant compositional and resulting property variations with regard to a trade-off between a lower shear strength (high percentage  $sp^2$  hybridisation) and a higher elastic modulus (high percentage of  $sp^3$  hybridisation). The variation in physical material properties with different hybridisation ratios ( $sp^2:sp^3$ ) is discussed in detail by Paul et al. [63]. Therefore, the range of DLC compositions endows it with a wide range of tribological properties, depending on the intended applications.

### 5. Concluding remarks

The frictional performance of some common cylinder bore material surfaces, including for high performance engines, were studied. Key surface parameters such as modulus of elasticity of surfaces, interfacial shear strength and surface energy are shown to have a strong correlation with measured nanoscale friction with AFM in LFM mode. Of the materials tested the electroplated Ni-SiC2 surface, used extensively in racing engine applications, is shown to exhibit lowest friction due its relatively low interfacial shear strength.

The increasingly used cylinder liner coating, DLC, is found to provide a mid-range coefficient of friction amongst the tested specimen. It is suggested that the reason for the variation between full scale engine performance of this material and the results shown here at the nanoscale could be due to the widely varying range of DLC coatings available in industry.

A more complete understanding of material behaviour in engine conditions could be accrued by determining boundary friction once

absorbed layers of surface active additives and contaminants have adhered or bonded to the surfaces in real cylinder applications as tribofilms. These ultra-thin films affect both the elastic modulus and the interfacial shear strength of the contact. The presented model provides a method for the evaluation of surfaces which is independent of such lubricant formulation variables. Future extension of this research would also need to extend the LFM work to investigation of these boundary films as shown by Chong et al. [51]. It is also important to note that the performance of surfaces for in-cylinder applications is also dependent on their finished topography, which includes the usual cross-hatching. There have been previous numerical analysis and experimental evaluation of cross-hatch angles, most suitable for cylinder liners [10,14,67].

## Acknowledgment

The authors would like to express their gratitude to the Engineering and Physical Sciences Research Council (EP/L014998/1) for the funding extended to this project under the CDT-ei scheme. The authors also acknowledge use of facilities within the Loughborough Materials Characterisation Centre (LMCC).

## References

- [1] King J. The King Review of low-carbon cars: Part I: the potential for CO2 reduction. UK: Office of Public Sector Information, HM Treasury, HMSO; 2007.
- [2] Holmberg K, Andersson P, Erdemir A. Global energy consumption due to friction in passenger cars. *Tribol Int* 2012;47:221–34.
- [3] Uras HM, Patterson DJ. Measurement of piston and ring assembly friction instantaneous IMEP method. 1983. SAE Technical Paper, No. 830416.
- [4] Fitzsimons B. Introduction to the importance of fuel efficiency and role of the Encyclopaedic research project. In: IMechE seminar: a drive for fuel efficiency, Loughborough; 2011.
- [5] Tung SC, McMillan ML. Automotive tribology overview of current advances and challenges for the future. *Tribol Int* 2004;37:517–36.
- [6] Sandford M, Allen J, Tudor R. Reduced fuel consumption and emissions through cylinder deactivation. SAE Int 1998. Pap No 984014.
- [7] Bewsher SR, Turnbull R, Mohammadpour M, Rahmani R, Rahnejat H, Offner G, et al. Effect of cylinder de-activation on the tribological performance of compression ring conjunction. *Proc IMechE, Part J J Eng Tribol* 2017. 1350650116684985.
- [8] Mohammadpour M, Rahmani R, Rahnejat H. Effect of cylinder deactivation on the tribo-dynamics and acoustic emission of overlay big end bearings. *Proc IMechE, Part K J Multi-body Dyn* 2014;228(2):138–51.
- [9] Bolander NW, Sadeghi F. Deterministic modeling of honed cylinder liner friction. *Tribol Trans* 2007;50(2):248–56.
- [10] Spencer A, Almqvist A, Larsson R. A semi-deterministic texture-roughness model of the piston ring-cylinder liner contact. *Proc IMechE, Part J J Eng Tribol* 2011; 225(6):325–33.
- [11] Morris N, Rahmani R, Rahnejat H, King PD, Fitzsimons B. The influence of piston ring geometry and topography on friction. *Proc IMechE, Part J J Eng Tribol* 2013; 227(2):141–53.
- [12] Truhan JJ, Qu J, Blau PJ. The effect of lubricating oil condition on the friction and wear of piston ring and cylinder liner materials in a reciprocating bench test. *Wear* 2005;259(7):1048–55.
- [13] Zhong M, Liu W, Zhang H. Corrosion and wear resistance characteristics of NiCr coating by laser alloying with powder feeding on grey iron liner. *Wear* 2006; 260(11):1349–55.
- [14] Howell-Smith S, Rahnejat H, King PD, Dowson D. Reducing in-cylinder parasitic losses through surface modification and coating. *Proc IMechE, Part D J Automob Eng* 2014;228(4):391–402.
- [15] Etsion I, Sher E. Improving fuel efficiency with laser surface textured piston rings. *Tribol Int* 2009;42(4):542–7.
- [16] Etsion I. Surface texturing for in-cylinder friction reduction. New Delhi (India): Woodhead Publishing Ltd; 2010.
- [17] Rahnejat H, Balakrishnan S, King PD, Howell-Smith S. In-cylinder friction reduction using a surface finish optimization technique. *Proc IMechE, Part D J Automob Eng* 2006;220(9):1309–18.
- [18] Godet M, Berthier Y, Leroy JM, Flamand L, Vincent L. Tribology series. Paper II (iii) coating design methodology, vol. 17. Elsevier Sci.; 1990. p. 53–9.
- [19] Bolander NW, Steenwyk BD, Sadeghi F, Gerber GR. Lubrication regime transitions at the piston ring-cylinder liner interface. *Proc IMechE, Part J J Eng Tribol* 2005; 219(1):19–31.
- [20] Ma MT, Sherrington I, Smith EH. Analysis of lubrication and friction for a complete piston-ring pack with an improved oil availability model. Part 1: circumferentially uniform film. *Proc IMechE, Part J J Eng Tribol* 1997;211(1):1–5.
- [21] Akain O, Newaz GM. Piston ring-cylinder bore friction modeling in mixed lubrication regime: part 1-analytical results. *Trans ASME, J Tribol* 1999;123(1): 211–8.
- [22] Balakrishnan S, Rahnejat H. Isothermal transient analysis of piston skirt-to-cylinder wall contacts under combined axial, lateral and tilting motion. *J Phys, D Appl Phys* 2005;38(5):787.
- [23] Morris N, Rahmani R, Rahnejat H, King PD, Fitzsimons B. Tribology of piston compression ring conjunction under transient thermal mixed regime of lubrication. *Tribol Int* 2013;59:248–58.
- [24] Styles G, Rahmani R, Rahnejat H, Fitzsimons B. In-cycle and life-time friction transience in piston ring–liner conjunction under mixed regime of lubrication. *Int J Engine Res* 2014;15(7):862–76.
- [25] Noorman MT, Assanis DN, Patterson DJ, Tung SC, Tseregounis SI. Overview of techniques for measuring friction using bench tests and fired engines. 2000. SAE Technical Paper, No. 2000-01-1780.
- [26] Gore M, Morris N, Rahmani R, Rahnejat H, King PD, Howell-Smith S. A combined analytical-experimental investigation of friction in cylinder liner inserts under mixed and boundary regimes of lubrication. *Lubr Sci* 2017. <http://dx.doi.org/10.1002/ls.1369>.
- [27] Landman U, Luedtke WD, Nitzan A. Dynamics of tip-substrate interactions in atomic force microscopy. *Surf Sci* 1989;210:L177–84.
- [28] Ruan J-A, Bhushan B. Atomic-scale friction measurements using friction force microscopy: Part I – general: principles and new measurement techniques. *Trans ASME, J Tribol* 1994;116(2):378–88.
- [29] Leighton M, Nicholls T, De la Cruz M, Rahmani R, Rahnejat H. Combined lubricant–surface system perspective: multi-scale numerical–experimental investigation. *Proc IMechE, Part J J Eng Tribol* 2016. <http://dx.doi.org/10.1177/1350650116683784>.
- [30] Azadi M, Rouhaghdam AS. Nanomechanical properties of TiN/TiC multilayer coatings. *Strength Mater* 2014;46(1):121–31.
- [31] Sundararajan S, Bhushan B. Micro/nanotribology of ultra-thin hard amorphous carbon coatings using atomic force/friction force microscopy. *Wear* 1999;225: 678–89.
- [32] Lackner JM, Waldhauser W, Ebner R, Bakker RJ, Schöberl T, Major B. Room temperature pulsed laser deposited (Ti, Al) C x N 1 – x coatings—chemical, structural, mechanical and tribological properties. *Thin Solid Films* 2004;468(1): 125–33.
- [33] Bhushan B. Nano-to-microscale wear and mechanical characterization using scanning probe microscopy. *Wear* 2001;251(1):1105–23.
- [34] Carpick RW, Agrait N, Ogletree DF, Salmeron M. Variation of the interfacial shear strength and adhesion of a nanometer-sized contact. *Langmuir* 1996;12(13): 3334–40.
- [35] Bradley RS. The cohesive force between solid surfaces and the surface energy of solids. *Phil Mag J Sci* 1932;13(86):853–62. LXXIX.
- [36] Johnson KL, Kendall K, Roberts AD. Surface energy and the contact of elastic solids. *Proc Roy Soc, Ser A- Math, Phys Eng Sci* 1971;324(1558):301–13.
- [37] Derjaguin BV, Muller VM, Toporov YP. Effect of contact deformations on the adhesion of particles. *J Colloid Interface Sci* 1975;53(2):314–26.
- [38] Maugis D. Adhesion of spheres: the JKR-DMT transition using a Dugdale model. *J Colloid Interface Sci* 1992;150(1):243–69.
- [39] Johnson KL, Greenwood JA. An adhesion map for the contact of elastic spheres. *J Colloid Interface Sci* 1997;192(2):326–33.
- [40] Tabor D. Surface forces and surface interactions. *J Colloid Interface Sci* 1977;58(1): 2–13.
- [41] Enachescu M, Van den Oetelaar RJA, Carpick RW, Ogletree DF, Flipse GFJ, Salmeron M. Observation of proportionality between friction and contact area at the nanometer scale. *Tribol Lett* 1999;7(2–3):73.
- [42] Bowden FP, Tabor D. The friction and lubrication of solids. Clarendon, UK: Oxford University Press; 1950.
- [43] Lantz MA, O'shea SJ, Welland ME, Johnson KL. Atomic-force-microscope study of contact area and friction on NbSe 2. *Phys Rev B* 1997;55(16):10776.
- [44] Riedo E, Lévy F, Brune H. Kinetics of capillary condensation in nanoscopic sliding friction. *Phys Rev Lett* 2002;88(18):185505.
- [45] Teodorescu M, Rahnejat H. Dry and wet nano-scale impact dynamics of rough surfaces with or without a self-assembled monolayer. *Proc IMechE, Part N J Nanoeng Nanosys* 2007;221(2):49–58.
- [46] Christenson HK. Adhesion between surfaces in undersaturated vapors—a reexamination of the influence of meniscus curvature and surface forces. *J Colloid Interface Sci* 1988;121(1):170–8.
- [47] Tambe NS, Bhushan B. Friction model for the velocity dependence of nanoscale friction. *Nanotechnology* 2005;16(10):2309–24.
- [48] Tambe NS, Bhushan B. A new atomic force microscopy based technique for studying nanoscale friction at high sliding velocities. *J Phys D Appl Phys* 2005;38(5):764–73.
- [49] Fisher LR, Israelachvili JN. Direct measurement of the effect of meniscus forces on adhesion: a study of the applicability of macroscopic thermodynamics to microscopic liquid interfaces. *Colloids Surfaces* 1981;3(4):303–19.
- [50] Israelachvili JN. Intermolecular and surface forces. London-New York: Academic press; 2011.
- [51] Chong W, Rahnejat H. Nanoscale friction as a function of activation energies. *Surf Topogr Metrol Prop* 2015;3:044002.
- [52] Buenavieja C, Ge S, Rafailovich M, Overney R. Atomic force microscopy calibration methods for lateral force, elasticity, and viscosity. In: MRS proceedings, vol. 522. Cambridge Univ. Press; 1998. p. 187.
- [53] Ahimou F, Semmens MJ, Novak PJ, Haugstad G. Biofilm cohesiveness measurement using a novel atomic force microscopy methodology. *Appl Environ Microb* 2007; 73(9):2897–904.
- [54] Carpick RW, Agrait N, Ogletree DF, Salmeron M. Variation of the interfacial shear strength and adhesion of a nanometer-sized contact. *Langmuir* 1996;12(13): 3334–3340Crossref.

- [55] Hues SM, Draper CF, Colton RJ. Measurement of nanomechanical properties of metals using the atomic force microscope. *J Vac Sci Tech B* 1994;13(3): 2211–4.
- [56] Oliver WC, Pharr GM. An improved technique for determining hardness and elastic modulus using load and displacement sensing indentation experiments. *J Mater Res* 1992;7(06):1564–83.
- [57] Hutter JL. Comment on tilt of atomic force microscope cantilevers: effect on spring constant and adhesion measurements. *Langmuir* 2005;21(6):2630–2.
- [58] Agarwal DK, Maheshwari N, Mukherji S, Rao VR. Asymmetric immobilization of antibodies on a piezo-resistive micro-cantilever surface. *RSC Adv* 2016;6(21): 17606–16.
- [59] Demas NG, Erck RA, Ajayi OO, Fenske GR. Tribological studies of coated pistons sliding against cylinder liners under laboratory test conditions. *Lubr Sci* 2012;24(5): 216–27.
- [60] Tabor D. The role of surface and intermolecular forces in thin film lubrication. *Tribol Ser* 1981;7:651–82.
- [61] Sutcliffe MJ, Taylor SR, Cameron A. Molecular asperity theory of boundary friction. *Wear* 1978;51(1):181–92.
- [62] Homola AM, Israelachvili JN, McGuiggan PM, Gee ML. Fundamental experimental studies in tribology: the transition from “interfacial” friction of undamaged molecularly smooth surfaces to “normal” friction with wear. *Wear* 1990;136(1): 65–83.
- [63] Paul R, Das SN, Dalui S, Gayen RN, Roy RK, Bhar R, et al. Synthesis of DLC films with different sp<sup>2</sup>/sp<sup>3</sup> ratios and their hydrophobic behaviour. *J Phys, D Appl Phys* 2008;41(5):055309.
- [64] Girifalco LA. Interaction potential for C60 molecules. *J Phys Chem* 1991;95(14): 5370–7.
- [65] Diebold U. The science of titanium dioxide. *Surf Sci Rep* 2003;48:53–229.
- [66] Zhong W, Overney G, Tomanek D. Structural properties of Fe crystals. *Phys Rev B* 1993;47(1):95.
- [67] Michail SK, Barber GC. The effects of roughness on piston ring lubrication Part I: model development. *Tribol Trans* 1995;38(1):19–26.